Applied Surface Science 532 (2020) 147335

Contents lists available at ScienceDirect

Applied Surface Science

journal homepage: www.elsevier.com/locate/apsusc

Hydrogen generation by ammonia decomposition over Co/CeO_2 catalyst: Influence of support morphologies

Chuanqing Huang[a,1], Yingzhi Yu[b,1], Xiaoyue Tang[a], Zeyu Liu[a], Jin Zhang[a], Chuanzhen Ye[a], Yong Ye[a,*], Rongbin Zhang[b,*]

[a] School of Chemistry and Chemical Engineering, South China University of Technology, Guangzhou 510006, China
[b] Key Laboratory of Jiangxi Province for Environment and Energy Catalysis, Institute of Applied Chemistry, College of Chemistry, Nanchang University, Nanchang 330031, China

ARTICLE INFO

Keywords:
Cobalt catalysis
Morphology effect
Ammonia decomposition
CeO_2

ABSTRACT

The fabrication of nanomaterial is a crucial issue in heterogeneous catalysis for on-site generation of hydrogen in proton exchange membrane fuel cell to achieve excellent performance for ammonia decomposition, and their effects of morphologies are still mysterious in the structure-reactivity relationship. In order to disclose it, three kinds of CeO_2 supports with three-dimensionally ordered mesoporous structure (3DOM), nanotubes (NT) and nanocubes (NC) were synthesized by nanocasting of a mesoporous silica KIT-6 template with cubic Ia3d symmetries, hydrothermal method with and without urea, respectively. Various characterization methods (XRD, BET, H_2-TPR, CO-TPD, TEM and XPS) were used to characterize the structure-reactivity relationship of catalysts. The Co/CeO_2-3DOM catalyst had higher H_2 producing rate (4.2 mmol/min·g_{cat}) than Co/CeO_2-NC (3.5 mmol/min·g_{cat}) and Co/CeO_2-NT (3.2 mmol/min·g_{cat}) under the reaction conditions of 500 °C and GHSV = 6000 mL/g_{cat}·h. The Co/CeO_2-3DOM catalysts presented Co nanoparticles with mean size of 5.2 nm, and the highest surface Co concentration (5.12%) and Ce^{3+}/Ce^{4+} ratio (0.53). Its high activity is attributed to higher surface area and more surface oxygen vacancies. The specific surface area and surface oxygen vacancy are significantly affected by the morphology of CeO_2 support. The more mechanism insight of the structure-activity relationship for ammonia decomposition has been revealed.

1. Introduction

Hydrogen storage technology is very important for utilization of hydrogen energy. Many kinds of hydrogen storage materials (including substances with the ability to absorb hydrogen, or hydrogen-containing compounds) have been studied so far [1,2]. Among those hydrogen resources, the on-site generation of CO_x-free hydrogen from ammonia decomposition directly fed to proton exchange membrane (PEM) fuel cells is especially considering [3]. This is due to conversion of ammonia to hydrogen and nitrogen without production of CO_x, which causes global warming (CO_2) and degrades cell electrodes (CO). Ammonia can be stored as liquid at 0.8 MPa (293 K). Moreover, it has a high gravimetric (17.8 wt% H_2), volumetric (121 kg H_2·m^{-3} in the liquid) H_2 density and energy density (3000 Wh·kg^{-1}). In addition, ammonia can be produced on an industrial scale through Haber-Bosch process [4,5]. Ammonia has not been widely used as an intermediate of hydrogen storage and transportation, because there is no effective catalyst to decompose ammonia into nitrogen and hydrogen [6,7]. Therefore, development of catalysts to efficiently attain hydrogen through on-site generation from ammonia at low temperature is critically important for mobile and remote applications.

Nowadays, many researchers have focused on Ru-[8–11], Ni-[11,12], Fe-[11,13] and Co-[14–17] based catalysts for ammonia decomposition. The high cost of Ru metal restricts the large-scale applications of Ru-based catalysts with high catalytic activity. Therefore, looking for a non-noble metal to replace Ru metal is necessary for practical applications. Amongst these transition metal based catalysts, the nitrogen binding energy of Co-based catalysts is the closest to the ideal value, so it has great potential for practical application [18]. Due to the relative low cost and its nitrogen adsorption energy, cobalt has also been explored as an alternative to ruthenium for hydrogen production via the ammonia decomposition reaction. For example, Dilek et al. [19] reported that cobalt incorporated silicate structured catalysts were prepared with sodium silicate using different cobalt precursors to

* Corresponding authors.
E-mail addresses: yeyong@suct.edu.cn (Y. Ye), rbzhang@ncu.edu.cn (R. Zhang).
[1] These authors contributed equally.

https://doi.org/10.1016/j.apsusc.2020.147335
Received 3 April 2020; Received in revised form 23 June 2020; Accepted 21 July 2020
Available online 28 July 2020
0169-4332/

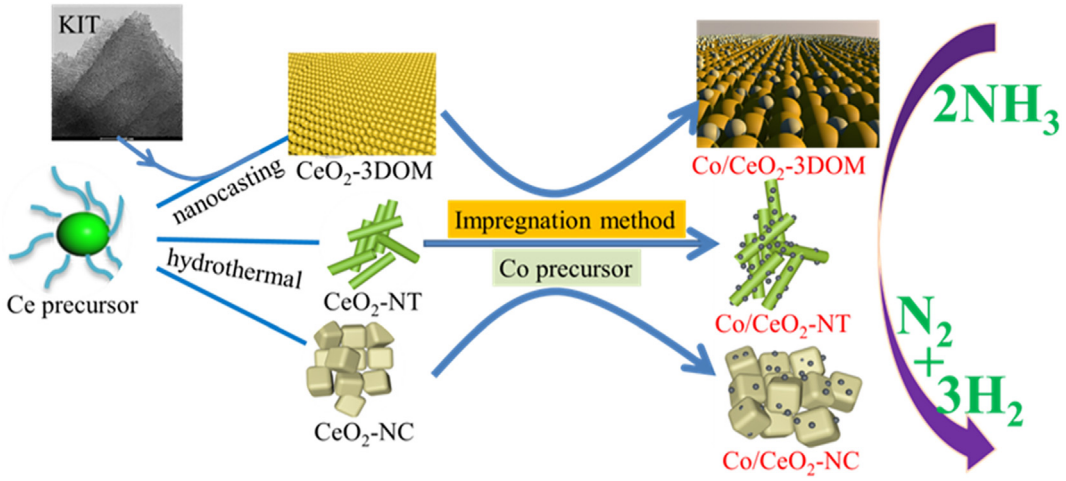

Scheme 1. Schematic diagram to illustrate the CeO_2 with different morphology supported Co catalysts for ammonia decomposition to hydrogen.

see the effects of cobalt precursors on the hydrogen production from ammonia. They confirmed that Co_3O_4 crystal was the main form of cobalt species in the structure of all the catalysts after their calcination at 550 °C. Podila et al. [15] revealed that high activity could be obtained by tailoring the alkaline strength of the mixed oxides as supports. The enrichment in activity of Co-based catalysts could be attributed to the increase of support basicity. Li et al. [14] found that the catalytic activity of cobalt nanoparticles embedded in a porous carbon matrix showed an obvious decrease with the increase of Co particle size. However, the methanation process of carbon matrix support at temperatures above 550 °C is an inherent disadvantage. Subsequently, the development of highly active Co-based catalysts for ammonia decomposition becomes a major aspect of research in this field.

CeO_2 can be used as the catalyst, support, or promoter for the catalytic ammonia decomposition [9,20,21]. Since ammonia decomposition is a structural sensitive reaction, extensive studies have focused on the effect of particle sizes, support components and promoters on ammonia decomposition [10,13–16,20,22,23]. These factors are related to the parameters of the active site, but it is not enough to understand the relationship between the structure and the active sites. The control of morphology provides a possible way for deep understanding of the structure-reactivity relationship. The structure-morphology-performance relationship of ammonia decomposition by adjusting the morphology of Co/CeO_2 catalyst has not been reported so far.

Therefore, different morphologies of CeO_2 with three-dimensional ordered mesoporous, nanocubes and nanotubes were designed as the support to evaluate the ammonia decomposition activity in this research. Meanwhile, the structure and surface properties of Co/CeO_2 catalysts were revealed by various physicochemical characterization (such as N_2 physisorption (BET), transmission electron microscopy (TEM), X-ray power diffraction (XRD), temperature-programmed reduction of hydrogen (H_2-TPR), temperature-programmed desorption of carbon (CO-TPD) and X-ray photoelectron spectroscopy (XPS)). The relationship between structure-morphology-performance for ammonia decomposition has been expounded.

2. Experimental

2.1. Catalyst preparation

Highly ordered mesoporous silica (designated as KIT-6) was synthesized by the Pluronic P123 triblock copolymer method [24]. Under stirring conditions, conc. HCl (11.8 g, 37%) was dissolved in 217 g of deionized water. Pluronic P123 (6 g, $EO_{20}PO_{70}EO_{20}$, Aldrich) was added to the solution and stirred for 12 h. n-butanol (6 g) and TEOS (12.9 g, Aldrich 98%) were added to the above mixture successively. After stirring for 24 h, the milky suspension was transferred to an autoclave and annealed at 100 °C for 24 h. After cooling to room temperature, the solid products were washed with the ethanol-HCl mixture, then dried at 100 °C and calcined at 550 °C for 5 h to remove the template completely. The white KIT-6 powder (2 g) was obtained.

Three-dimensionally ordered mesoporous CeO_2 was fabricated using KIT-6 as a hard template. Typically, an appropriate amount of $Ce(NO_3)_3{\cdot}6H_2O$ was added to the 15 mL ethanol solution. After the dissolution of $Ce(NO_3)_3{\cdot}6H_2O$, KIT (0.5 g) was added and stirred to dry at room temperature. Under air atmosphere, the precursor@KIT-6 composite was heated at a rate of 1 °C/min for 5 h at 550 °C. To remove the silica template, the obtained solid powder was next washed with 2 M NaOH solution. After dried at 100 °C, the product (0.7 g) was denoted as CeO_2-3DOM.

The CeO_2-nanotube (CeO_2-NT) was prepared by a hydrothermal method according to the literature [25–27]. The synthetic procedure is as follows: under the condition of magnetic stirring, $Ce(NO_3)_3{\cdot}6H_2O$ (3.4 g) and urea (7.2 g) were successively dissolved in 160 mL deionized water, and then transferred to an autoclave at 80 °C for 24 h. The $Ce(OH)CO_3$ was obtained after washing, filtration and drying of precipitate. $Ce(OH)CO_3$ (0.5 g) was dissolved in 80 mL NaOH (2.4 M) solution. The mixture was transferred to the Teflon reactor for 120 °C reaction for 12 h after stirring for 30 min. Light yellow CeO_2-NT powder (0.4 g) was obtained after filtration, washing and drying.

The CeO_2-cubes (CeO_2-NC) synthesis is similar to our previous work [26,27]. Briefly, under the condition of vigorous stirring, $Ce(NO_3)_3{\cdot}6H_2O$ (1.72 g) and 60 mL NaOH (10 M) solution were successively dissolved in 20 mL deionized water to form a milky slurry. The mixture was transferred to the autoclave and held in 130 °C for 48 h. CeO_2-NC sample (0.5 g) were obtained by filtration, washing and drying.

Appropriate amount of $Co(NO_3)_3{\cdot}6H_2O$ solution was impregnated on CeO_2-3DOM, CeO_2-NC and CeO_2-NT supports. After vacuum drying at 60 °C, Co/CeO_2 catalysts with different morphologies were obtained after calcination at 600 °C in an air atmosphere for 5 h. The mass ratio of Co for three Co/CeO_2 catalysts was fixed at 5 wt%. The design route of CeO_2 with different morphology supported Co catalysts for ammonia decomposition to hydrogen is illustrated in Scheme 1.

2.2. Catalyst characterization

2.2.1. XRD

X-ray diffraction (XRD) patterns of the prepared catalysts were completed on a Bruker AXS D8 Focus diffractometer. The conditions was as follows: Cu Kα (λ = 0.154056 nm) radiation at 40 kV and 30 mA with 3 mm scattering scale, diffraction data (2θ = 10–80°) at a

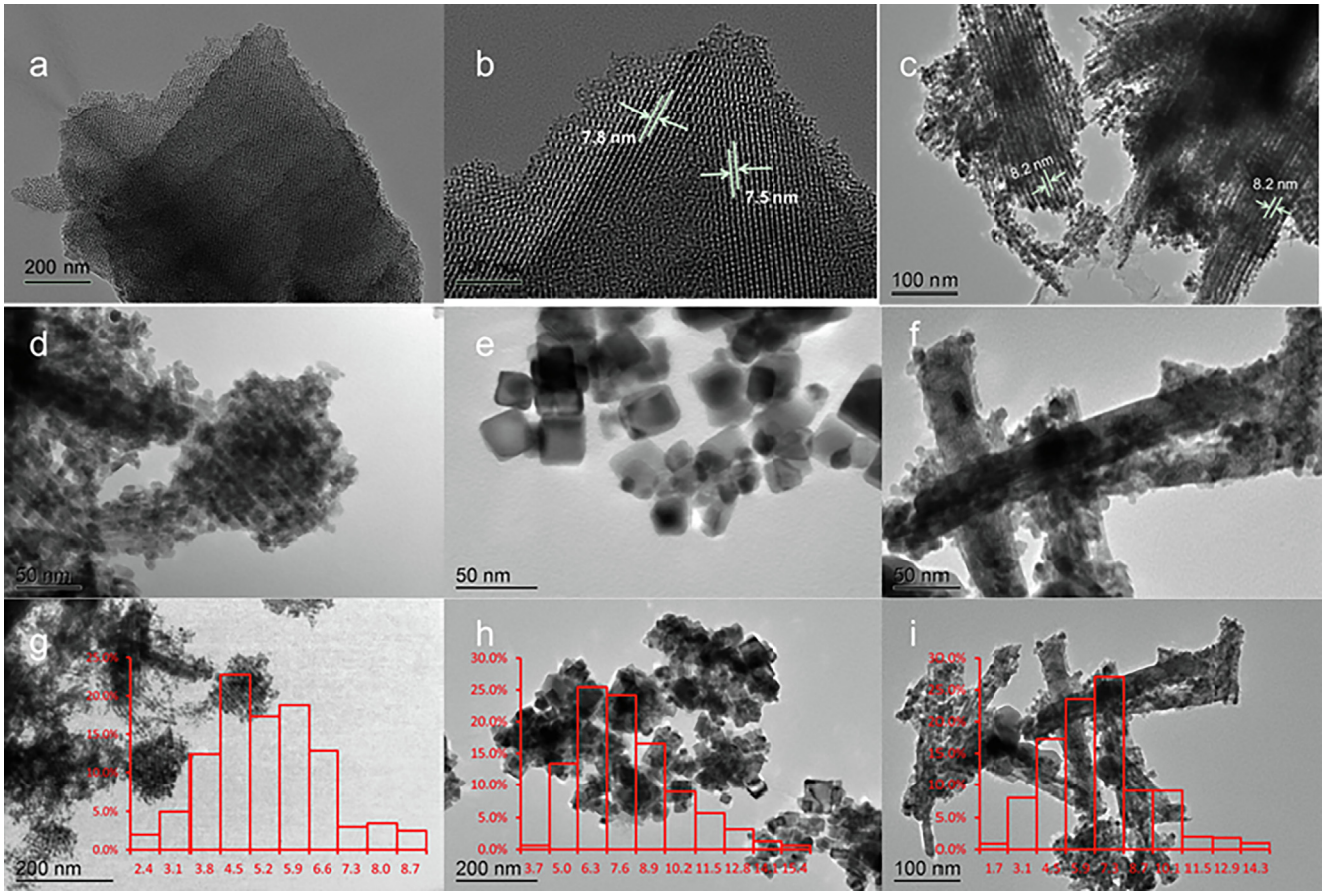

Fig. 1. TEM images of KIT-6 (a, b), CeO_2-3DOM (c), Co/CeO_2-3DOM (d, g), Co/CeO_2-NC (e, h) and Co/CeO_2-NT (f, i).

scanning rate of 4°/min. Based on the CeO_2 (111) and Co_3O_4 (311) diffraction peaks, the Scherrer equation (1) was used to calculate the crystal size of CeO_2 and Co_3O_4, respectively.

$$D = \frac{k\lambda}{\beta\cos\theta} \quad (1)$$

where k is the Scherrer constant, β is full width at half of the maximum intensity, and θ stands for the diffraction angle.

2.2.2. N_2 sorption

A Micromeritics ASAP2020 equipment (Micromeritics, USA) was used to measure the surface area and pore size distributions of bare CeO_2 support as well of Co/CeO_2 catalysts. All the samples were degassed at 200 °C for 2 h prior to measurement.

2.2.3. TEM

A transmission electron microscope (TEM, JSM-2010, JEOL, Japan) was used for imaging of the samples. After dispersing the sample to the acetone solution by ultrasound for 0.5 h, the mixture was impregnated and dispersed to the carbon-film-coated copper grids.

2.2.4. H_2-TPR

A Micromeritics 2920 system (Autochem II, Micromeritics, USA) equipped with a TCD detector and quartz tubular reactor was used to detect the reducibility of catalysts. The procedure was as follows: 50 mg catalyst was placed in a quartz tube and degassed at 200 °C for 1 h to remove impurities adsorbed in the catalyst. After cooled to room temperature, the sample was heated from room temperature to 800 °C at a flow of 10% H_2/Ar (30 mL/min) and a rate of 10 °C/min.

2.2.5. CO-TPD

Temperature-programmed desorption of CO (CO-TPD) was performed on a reactor with the same equipment of TPR detection to measure the exposed Co surface area. The catalyst (50 mg) was loaded into a quartz tube for each test. Prior to the pulse CO chemisorption measurement, the catalyst was reduced at 600 °C for 2 h in 10% H_2 (balance with Ar), and then cooled down to room temperature in He flow. Then, the 10% CO/He flow was introduced for a period of 0.5 h at room temperature. After CO chemisorption was performed under cryogenic conditions, pure He was introduced to remove redundant CO. Heating treatment was performed with a 10 °C/min ramp from room temperature to 800 °C. CO uptake was measured using a gas chromatography equipped with TCD detector. Co metal surface area was calculated by assuming a stoichiometry of 1:1 for CO:Co.

2.2.6. XPS

An ESCALAB250 Xi system (XPS, Thermo Fisher Scientific, USA) with monochromatic Al Ka (1486.6 eV) as excitation source was used to determine the binding energies (BEs) of surface species. The C1s peak (284.8 eV) from adventitious carbon was as a reference of the binding energy. The surface composition and chemical state were analyzed by the binding energies of the Ce 3d, Co 2p and O 1s photoelectron peaks.

2.3. Catalytic activity measurements

Catalytic activities were evaluated in a quartz tube fixed bed reactor under pure ammonia (atmospheric pressure, GHSV = 6000 mL/g_{cat}·h). Prior to the reaction, all catalysts (100 mg) were in-situ reduction by a pure H_2 flow at 600 °C for 2 h, followed by a purge of residual hydrogen with Ar gas. After the temperature drops to 300 °C, the Ar flow was switched to ammonia gas, and then the temperature rises to 600 °C at

intervals of 50 °C. The data at each temperature was obtained continuously under the steady state. The on-line gas chromatography (GC-9790II, Zhejiang FULI Analytical Instrument Co., Ltd., China) equipped with a TCD detector was used to analyze the composition of gases. The gas chromatographic condition was as follows: Ar gas as carrier gas, Poropak N column. The total amount of ammonia in feed gas and unconverted amount of ammonia were denoted as $A_{NH_3,in}$ and $A_{NH_3,out}$, respectively. The conversion of ammonia was obtained by formula (2).

$$X_{NH_3} = \frac{(A_{NH_3,in} - A_{NH_3,out})}{A_{NH_3,in}} \times 100\% \quad (2)$$

In the desired temperature value, all data were done in triplicate after the reaction reached steady state. The H_2 formation rate was calculated from the Eq. (3), where V_{NH3} refers to the amount at a flow rate, as follow:

$$H_2 \text{ formation rate } (\text{mmol/min}\cdot g_{cat}) = \frac{\frac{V_{NH_3}}{22.4}\cdot Conv_{(NH_3)}\%.\ 1.5}{m_{cat}} \quad (3)$$

3. Results and discussion

3.1. Structure and morphology of the CeO_2 catalysts

The TEM images of the prepared KIT-6, Co/CeO_2-3DOM, Co/CeO_2-NC and Co/CeO_2-NT catalysts were illustrated in Fig. 1. Among all of them, Fig. 1a and b showed that the KIT-6 template was successfully prepared with a well-ordered and alternate pore channel structure with an aperture of 7.5–7.8 nm. Fig. 1c showed that CeO_2 had a three-dimensional ordered mesoporous structure after removing the KIT-6 template. These alignments of the cylindrical channel with cubic *Ia3d* symmetries structure were distributed along the direction of [1 1 0] or [0 0 1]. The average diameter of these particles for Co/CeO_2-3DOM catalyst was 5.2 nm. The uniform cube morphology with size range of 13.1 nm to 37.6 nm was presented in Fig. 1e and h. The average diameter of cobalt nanoparticles for Co/CeO_2-NC (Fig. 1h) catalysts was 7.8 nm. The mean diameter of CeO_2 nanotubes was around 34.5 nm in Fig. 1i. After loading the cobalt metal, the cobalt nanoparticles with an average diameter of 6.6 nm were dispersed the surface of the CeO_2 nanotubes in the Fig. 1f and i. The (1 1 0) and (1 0 0) crystal planes are the main exposed crystal planes of CeO_2 nanotubes and CeO_2 nanocubes, respectively [26,27]. It confirms that the desired morphology has been successfully synthesized in our experiment.

Fig. 2 showed the powder XRD pattern of the as-prepared CeO_2 supports and the corresponding supported Co catalysts. The characteristic peaks of a typical crystalline fluorite structure (PDF# 34-0394) appeared in all catalysts at 2θ = 28.6°, 32.9°, 47.5°, 56.3°, 59.1°, 69.4°, 76.7°, and 79.1°, corresponding to the (1 1 1), (2 0 0), (2 2 0), (3 1 1), (2 2 2), (4 0 0), (3 3 1) and (4 2 0) planes, respectively [28]. By Scherrer equation calculation, the crystallite size of CeO_2-3DOM, CeO_2-NC and CeO_2-NT supports were 12.7 nm, 23.2 nm and 10.9 nm, respectively. After Co was cross-linked with CeO_2 supports, the structural characteristic peak of bare CeO_2 did not modify notably, indicating that thermal treatment does not lead to a collapse of the fluorite structure of bare CeO_2. Meanwhile, the weaker peak of Co_3O_4 (3 1 1) at 37.1° (PDF# 43–1003) appeared in Fig. 2b, indicating that Co_3O_4 is the main crystalline structure of cobalt metal after calcination. The order of Co_3O_4 crystalline size of the three catalysts was as follows: Co/CeO_2-NC (39 nm) > Co/CeO_2-3DOM (33 nm) > Co/CeO_2-NT (19 nm). For the reduced Co/CeO_2 samples, besides the diffraction rays of CeO_2 support, Co metal peak did not appear. However, a very weak peak of Co_3O_4 could be observed. When the catalyst was exposed to air, the Co metal was oxidized again after reduction by hydrogen. The used Co/CeO_2-3DOM catalyst after stability test at 600 °C was also characterized by XRD. It could be realized from the Fig. 2 that the peak of the Co/CeO_2-3DOM catalyst did not change significantly, indicating that the Co/CeO_2-3DOM catalyst is stable.

The N_2 adsorption-desorption isotherms and pore size distribution of KIT-6 and Co/CeO_2 with different morphologies were shown in Fig. 3. According to the IUPAC classification, the N_2 adsorption-desorption isotherms of KIT-6 belonged to type IV and H1 hysteresis loop in Fig. 3a. More physical properties of the as-prepared samples were listed in Table 1. KIT-6 synthesized by a triblock copolymer ($EO_{20}PO_{70}EO_{20}$)–butanol mixture for the structure direction method had a BET surface area of 1243 m^2/g, a pore volume of 1.53 cm^3/g and an average pore size of 6.7 nm. These characteristics indicate that KIT-6 has a large channel-like pores structure [29]. TEM images (Fig. 1a and b) also demonstrated that KIT-6 had this unique structure. For Co/CeO_2-NC and Co/CeO_2-NT catalysts, the adsorption-desorption curves of type IV with a H1 hysteresis loop was presented in Fig. 3b. In the etching process, the mesoporous structure of CeO_2-3DOM emerged after the silica template was washed off from the ceria/silica composite. Therefore, the mesopores in the CeO_2 matrix resembles the same narrow form of silica walls which are channel-like. Nitrogen physisorption isotherms of Co/CeO_2-3DOM catalyst exhibited a type IV isotherm with a broad capillary condensation range starting at about P/P_0 = 0.6 and extending almost to P/P_0 = 1, indicative of a high fraction of textural porosity [24]. After metal nanoparticles loading onto the CeO_2-3DOM support, the specific surface area and pore volume were significantly reduced, indicating that the Co nanoparticles cover and/or enter the pore channel.

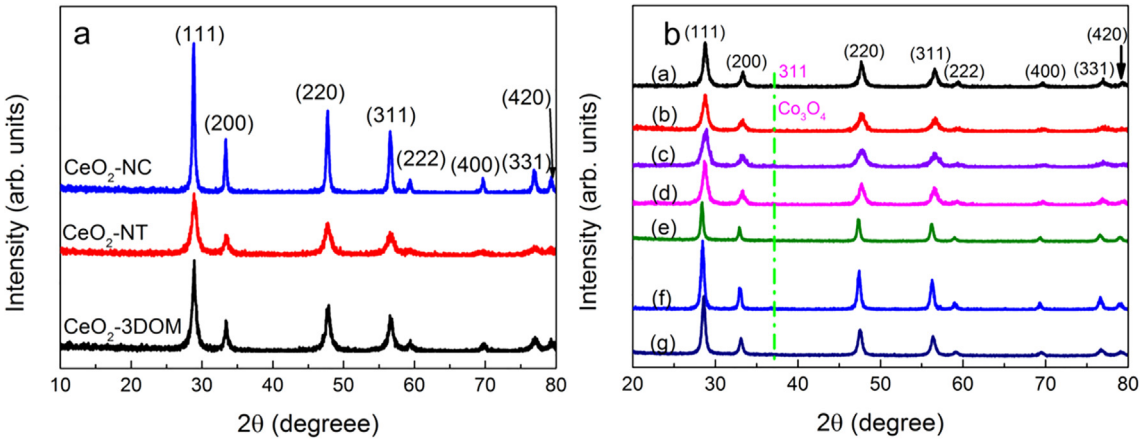

Fig. 2. a. XRD patterns of CeO_2-3DOM, CeO_2-NC, CeO_2-NT supports; b. XRD patterns of Co/CeO_2-3DOM (a), reduced Co/CeO_2-3DOM (b), used Co/CeO_2-3DOM (c), Co/CeO_2-NT (d), reduced Co/CeO_2-NT (e), Co/CeO_2-NC (f), reduced Co/CeO_2-NC (g) catalysts.

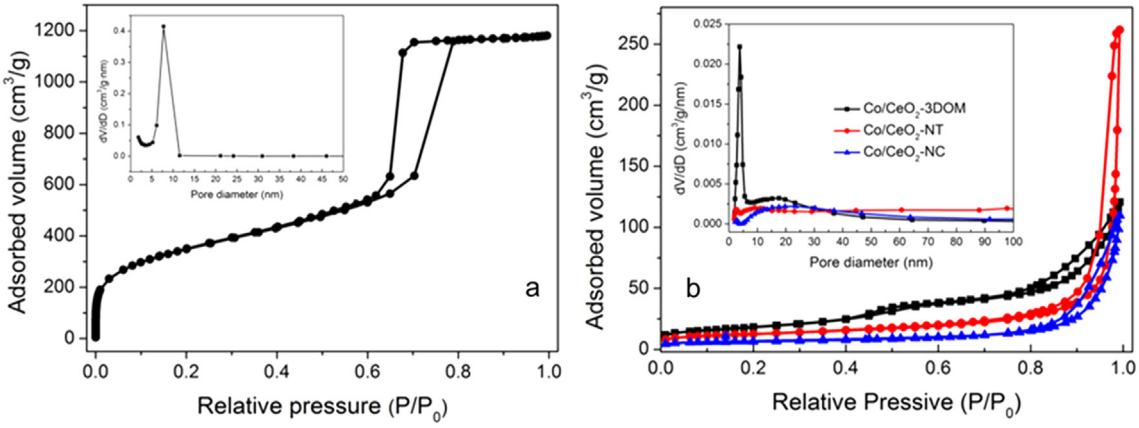

Fig. 3. N_2 physisorption isotherm of (a) KIT-6 and (b) Co/CeO_2-3DOM, Co/CeO_2-NC, Co/CeO_2-NT at −196 °C. Pore size distribution from BJH desorption (Inset) of (a) KIT-6 and (b) Co/CeO_2-3DOM, Co/CeO_2-NC, Co/CeO_2-NT.

Table 1
BET surface areas, pore volume, and average pore diameters (BJH) for KIT-6, Co/CeO_2-3DOM, Co/CeO_2-NC, Co/CeO_2-NT catalysts.

Samples	$S_{(BET)}$ (m^2/g)	Pore volume (cm^3/g)	Pore diameter (nm)
KIT	1243	1.53	6.7
CeO_2-3DOM	90	0.24	9.4
CeO_2-NT	45	0.08	5.9
CeO_2-NC	36	0.05	23.1
Co/CeO_2-3DOM	64	0.19	10.7
Co/CeO_2-NT	41	0.07	6.0
Co/CeO_2-NC	20	0.03	28.5

3.2. Surface chemical properties and reduction behavior analysis

The surface chemical compositions and chemical states of Co/CeO_2 catalysts were revealed by XPS in the Fig. 4. As shown in Fig. 4a, except for Ce, Co and O elements, the XPS survey spectra revealed that there were no other redundant elements on the surface. Fig. 4b showed the XPS spectra of Ce 3d of CO/CeO_2 catalysts with different morphologies. All catalysts were divided into eight deconvoluted peaks after deconvolution. The peak at 882.5, 888.6, 898.4, 900.9, 907.5 and 916.6 eV belonged to Ce^{3+}3d binding energy, while the peak position of Ce^{4+}3d bond energy should located at 884.7 and 902.2 eV [27,30]. The Ce 3d of the mixed valence state indicates that the surface of CeO_2 support has redox property, which increases the oxygen migration on the surface through redox reactions of Ce^{3+}/Ce^{4+}. By integrating the peak area, the Ce^{3+}/Ce^{4+} ratio of Co/CeO_2-3DOM (0.53) was significantly higher than that of Co/CeO_2-NC (0.39) and Co/CeO_2-NT (0.33) catalysts. The O1s spectrum was used to further analyze the surface oxygen species. As shown in Fig. 4c, the Co/CeO_2-NC catalyst could be fitted into three peaks at BE = 528.9, 529.6 and 531.3 eV. Similarly, O1s spectra of Co/CeO_2-NT and Co/CeO_2-3DOM catalysts could be divided into three peaks (529.1, 530.0 and 531.6 eV) and two peaks (529.5 and 531.3 eV) after Gaussian function fitting, respectively. These peaks at 528.9–530 eV are attributed to lattice oxygen, while other peaks (531.3 and 531.6 eV) are attributed to surface adsorbed oxygen species [30,31]. Considering the integrated XPS peak area of lattice oxygen and surface adsorbed oxygen species, the order of the O_{ads}/O_{latt} was follows: Co/CeO_2-3DOM > Co/CeO_2-NC > Co/CeO_2-NT. Surface oxygen species are related to active species, therefore, the Co 2p profile on the catalyst surface was further analyzed. As shown in Fig. 4d, the Co 2p energy spectra of the three catalysts showed two bond energy peaks at 780 eV and 796 eV. After fractional peak fitting and analysis, the catalyst surfaces of Co^{3+} and Co^{2+} are corresponding to Co_2O_3 and CoO species, respectively [32,33]. This indicates that Co_3O_4 is the main active component after calcination. Table 2 further showed that the content of Co on the surface of Co/CeO_2-3DOM catalyst was significantly higher than that of the other two catalysts.

The relationship between active component and support was further characterized by H_2-TPR. The result was shown in Fig. 5. As for the CeO_2 supports, the reduction temperature of surface reactive oxygen species was 250–400 °C. The reduction temperature between 400 and 600 °C was due to the change process of bulk oxygen species. The high reduction temperature (over 600 °C) was attributed to the stable oxygen species [33,34]. CeO_2-3DOM catalyst obviously had the readily reduced oxygen species at 376 °C. The surface oxygen species was easier to use than other oxygen species. After Co-O-Ce crosslinking, the reduction peak of Co shifted to low temperature [32]. Co/CeO_2-NT (273 °C and 288 °C), Co/CeO_2-NC (251 °C and 271 °C) and Co/CeO_2-3DOM (311 °C and 362 °C) catalysts had two obvious reduction peaks. The low temperature region belonged to the process of Co^{3+} reduction to Co^{2+} ($Co_3O_4 \rightarrow CoO$). The high temperature reduction peak was attributed to the Co^{2+} reduction to Co^0 process ($CoO \rightarrow Co^0$). Based on TPR peaks area, the order of H_2 consumption was obtained: Co/CeO_2-3DOM (552.0×10^{-3} mmol/g_{cat}) > Co/CeO_2-NC (549.3×10^{-3} mmol/g_{cat}) > Co/CeO_2-NT (548.9×10^{-3} mmol/g_{cat}), which is in accordance with the catalytic activity results obtained from Fig. 7. Compared with the reduction peak of Co/CeO_2-3DOM catalyst, the reduction peak of Co/CeO_2-NC and Co/CeO_2-NT catalysts shifted to low temperature, indicating that Co/CeO_2-3DOM catalyst has stronger Ce-O-Co bond.

The desorption behavior of CO from the Co catalysts to explore the number of active sites was illustrated in Fig. 6. The desorption peaks of Co/CeO_2-NC, Co/CeO_2-NT and Co/CeO_2-3DOM catalysts were 102 °C, 86 °C and 98 °C, respectively. Based on the peak area of CO-TPD profiles and assumption of an adsorption of one per metal atom, the Co metal dispersion ratios of Co/CeO_2-3DOM, Co/CeO_2-NC and Co/CeO_2-NT catalysts were 39.0%, 37.0% and 30.8%, respectively. The turnover frequency was calculated by formula (4), here D and n_{total} represent the dispersion and the total amount of active metal respectively.

$$TOF_{H_2} = \frac{H_2 \text{ formation rate } (\text{mmol/min}\cdot g_{cat})}{n_{total} \times D} \quad (4)$$

As shown in Table 3, the TOF_{H2} of Co/CeO_2-3DOM catalyst (1.81 min^{-1}) was higher than that of Co/CeO_2-NC (1.68 min^{-1}) and Co/CeO_2-NT catalyst (1.16 min^{-1}).

3.3. Catalytic activity

Fig. 7 illustrated the catalytic performance of the Co/CeO_2-3DOM, Co/CeO_2-NC and Co/CeO_2-NT catalysts in the ammonia decomposition reaction ($2NH_3 \rightarrow 3H_2 + N_2 \Delta H = 46 kJ/mol$). At temperatures below 300 °C, the ammonia conversion rate was close for the three catalysts. Subsequently, with the increase of temperature, the ammonia

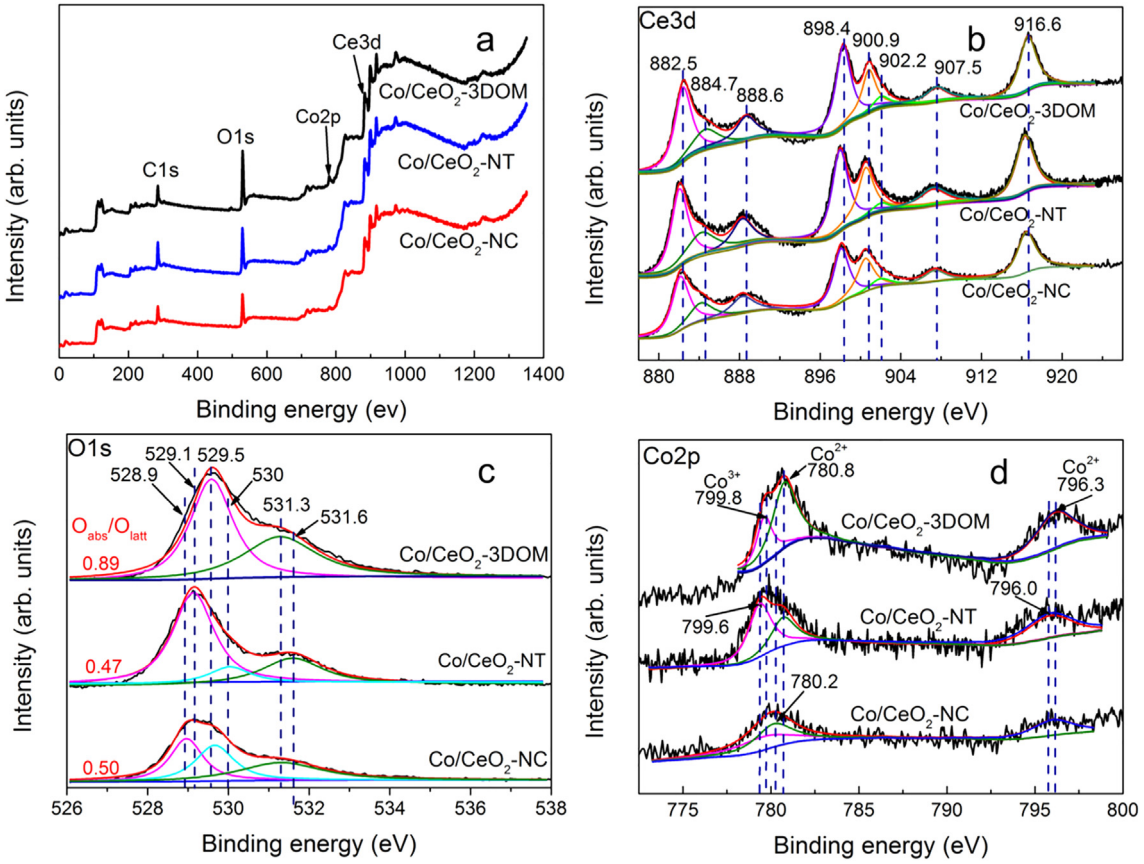

Fig. 4. (a) XPS survey spectra of Co/CeO_2-3DOM, Co/CeO_2-NT and Co/CeO_2-NC catalysts; XPS curve-fitting of the Ce 3d (b), O 1s (c) and Co 2p (d) photoelectron peaks in the Co/CeO_2-3DOM, Co/CeO_2-NT and Co/CeO_2-NC catalysts.

conversion rate of Co/CeO_2-3DOM catalyst with a Ce^{3+}/Ce^{4+} of 0.53 was significantly higher than that of Co/CeO_2-NC ($Ce^{3+}/Ce^{4+}=0.39$) and Co/CeO_2-NT ($Ce^{3+}/Ce^{4+}=0.33$) catalysts. In the test temperature range, the order of activity of the three catalysts was as follows: Co/CeO_2-3DOM > Co/CeO_2-NC > Co/CeO_2-NT.

Table 4 summarized the reported ammonia conversion rate and H_2 formation rate of Co-based catalysts [11,14–17,23,35,36]. Although the ammonia conversion and H_2 formation rates for Co/MWCNTs, CoO_x@C-700-A and CoX (X = Mn, Cr) and Co/SiO_2 catalysts were high, the activity of these catalysts was obtained under high cobalt metal loads. In the same cobalt content (5 wt%), the ammonia conversion and H_2 formation rate of Co/CeO_2-3DOM catalyst were higher than that of Co/MWCNTs, 5CMAl-2, 5CMCe-2 and $Co/MgO\text{-}La_2O_3$ catalysts. In addition, the ammonia decomposition activity of 5CoTi-NT (titanium nanotubes loaded 5 wt%Co) at 550 °C was 19%. In this study, the activity of Co/CeO_2-NT catalyst with similar nanotube structure at 550 °C was 67%.

The relationship between morphology and activity was further analyzed by Arrhenius equation ($\ln(\text{rate}) = \text{Constant} - \frac{Ea}{R}\frac{1}{T}$), where rate is referred to the H_2 formation rate, Ea is the activation energy, R is the universal gas constant, T is the temperature. As shown in the Fig. 8, the Ea of the three catalysts could be compared in the following order: Co/CeO_2-NT (69.0 kJ mol^{-1}) > Co/CeO_2-3DOM (64.7 kJ mol^{-1}) > Co/CeO_2-NC (63.5 kJ mol^{-1}). It is well known that the activation energy of the catalyst also represents the minimum

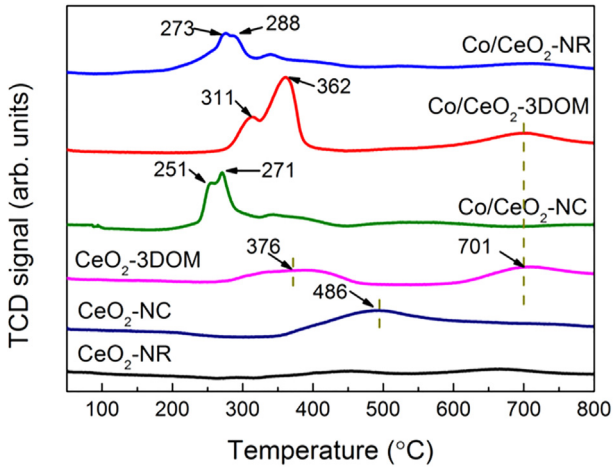

Fig. 5. Temperature program spectra of CeO_2-3DOM, CeO_2-NC, CeO_2-NT supports, Co/CeO_2-3DOM, Co/CeO_2-NC and Co/CeO_2-NT catalysts.

Table 2
Summary of the XPS data for Co/CeO_2-3DOM, Co/CeO_2-NC and Co/CeO_2-NT catalysts.

Catalyst	Co 2p BE (eV)	Surface Co concentration atomic %	O_{ads}/O_{latt}	Surface oxygen concentration atomic %	Ce^{3+}/Ce^{4+}
Co/CeO_2-NC	780.03	2.95	0.50	75.31	0.39
Co/CeO_2-NT	779.74	3.26	0.47	76.24	0.33
Co/CeO_2-3DOM	780.49	5.12	0.89	78.50	0.53

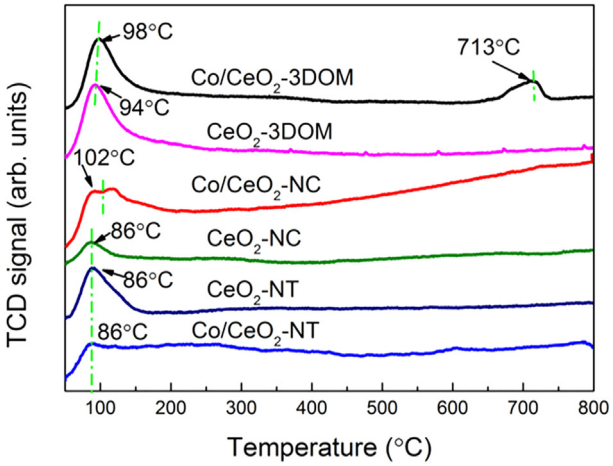

Fig. 6. CO-TPD profiles of CeO_2-3DOM, CeO_2-NC, CeO_2-NT, Co/CeO_2-3DOM, Co/CeO_2-NC and Co/CeO_2-NT catalysts.

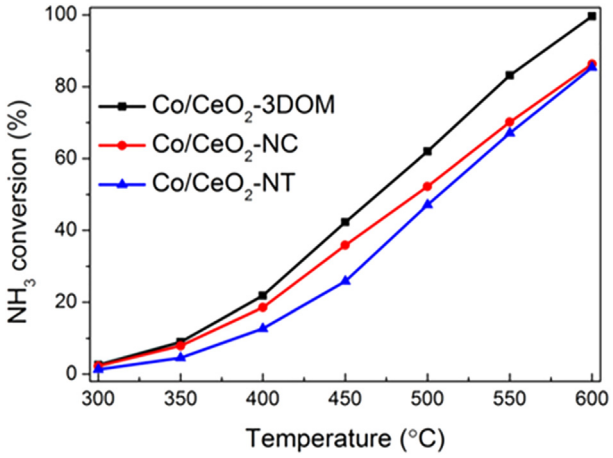

Fig. 7. Ammonia conversion as a function of reaction temperature over Co/CeO_2-3DOM, Co/CeO_2-NC and Co/CeO_2-NT catalysts.

energy barrier required to catalyze the reaction. It could be concluded from the characterization of the three catalysts that different morphologies form oxygen vacancies on the surface, resulting in different activation energies.

As shown in Fig. 9, the stability and reproducibility of the most active Co/CeO_2-3DOM catalyst were tested between 550 °C and 600 °C. It was obvious that the activity of the Co/CeO_2-3DOM catalyst remained stable after 72 h. The stability and reproducibility are critical for industrial applications of catalysts.

3.4. Structure-activity relationship

Multiple characterizations were employed to understand structure–activity relationship for ammonia decomposition. As shown in Figs. 2, 4, 5 and 6, these peak shapes of the three catalysts were similar, indicating similar structures and active sites during ammonia decomposition. So it could be seen from Fig. 7 that there was little difference in the initiation of catalytic activity and the trend of change. Traditionally, the size of the nanocatalysts is the key factor of the activity. It is generally accepted that the smaller the cobalt particle size, the higher the catalytic activity [14,35], which is so-called size-dependent catalytic chemistry. In this study, an approximate cobalt average particle of Co/CeO_2-3DOM catalyst was 5.2 nm of size. It seemed to agree with the high activity of the cobalt active sites. However, the particle size between these Co/CeO_2 catalysts with different morphology was similar in the Fig. 1. It indicates that the main factor of catalytic activity for Co/CeO_2 catalysts is not nanoparticle size.

Table 4
Ammonia conversion and H_2 formation rate over cobalt based catalysts at 500 °C.

Catalyst	Metal content (wt%)	GHSV (ml/g_{cat}·h)	Ammonia conversion (%)	H_2 formation (mmol/min·g_{cat})
Co/CNTs[36]	4.1	5000	8	0.5
Co/MWCNTs[16]	10	6000	74.6	5.0
Co/MWCNTs[43]	5	6000	60	4.0
CoO_x@C-700-A[14]	18.7	15,000	~55	8.8
CoX(X = Mn, Cr) [17]	94.8	24,000	35	9.4
5CMLa-2[15]	5	6000	48	3.2
5CMCe-2[15]	5	6000	40	2.7
5CMAl-2[15]	5	6000	8	0.5
Co/MgO-La_2O_3[23]	5	6000	60	4.0
Co/SiO_2[11]	66.8	30 000	13	4.3
10CoNaTi-NT[35]	6.8	6000	~18	0.35
5CoTi-NT[a][35]	5	6000	19	0.41
Co/CeO_2-3DOM	5	6000	62	4.2

[a] Measured at 550 °C.

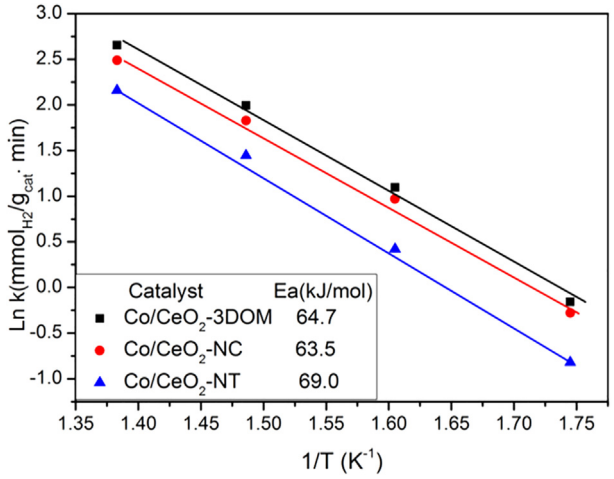

Fig. 8. The Arrhenius plots for ammonia decomposition over Co/CeO_2-3DOM, Co/CeO_2-NC and Co/CeO_2-NT catalysts.

Table 3
Summary of CO-uptake, H_2 formation rate and TOF values of the as-prepared samples.

Samples	CO-uptake (10^{-3} × mmol/g_{cat})[a]	H_2 formation rate (10^{-3} × mmol/min·g_{cat})[b]	TOF_{H2} (min^{-1})[c]
Co/CeO_2-3DOM	330.5	596.8	1.81
Co/CeO_2-NC	313.4	526.8	1.68
Co/CeO_2-NT	261.0	304.0	1.16

[a] Co-uptake data values were obtained by quantitatively analyzing the CO-TPD profiles.
[b] The H2 formation rate data of Co/CeO2 with different morphologies were obtained by formula (3) at 350 °C.
[c] The value of TOFH2 was calculated by formula (4) [42].

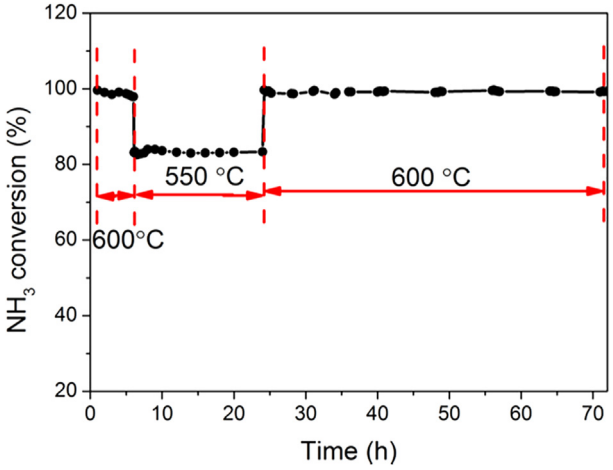

Fig. 9. Tests of stability and reproducibility over Co/CeO_2-3DOM catalyst at GHSV = 6 000 mL h^{-1} g_{cat}^{-1}.

The physical adsorption measurement in Fig. 2 and Table 1 showed that the Co/CeO_2-3DOM catalyst had a higher specific surface area than the Co/CeO_2-NC and Co/CeO_2-NT catalysts, and the specific surface area was directly changed by the controlled morphology of the CeO_2 support. It is well known that high specific surface area and large pore volume facilitate mass transfer in the process of ammonia decomposition. In addition, the high specific surface area provides more opportunities for the exposure of the active surface. From a kinetic point of view, as ammonia decomposition reaches dynamic equilibrium, the ammonia conversion rate is affected by the partial pressure of ammonia adsorbed on the active site. On the other hand, the cross-linking strength between active site and reactive facet could be characterized by H_2-TPR. Campbell et al. [37] proposed that the electronic metal-support interaction related to ceria was formed by chemical bonds to metal nanoparticles. Compared with Co/CeO_2-NC and Co/CeO_2-NR catalysts, it was obvious from Fig. 5 that the reduction peak of Co_3O_4 species of Co/CeO_2-3DOM catalyst shifted to high temperature. This means that the electronic metal-support interaction of the Co/CeO_2-3DOM catalyst is the strongest. Podila et al. [23] indicated that the observed high catalytic activity of 5CMLa-N_2 catalyst for ammonia decomposition was attributed to the increased cobalt support interaction. Although Co/CeO_2-NC catalyst has the best redox, it also demonstrates that its electronic metal-support interaction is weaker. The stronger electronic metal-support interaction for Co/CeO_2 catalysts is beneficial to prevent the agglomeration of active sites in the process of high temperature reaction. In addition, XPS showed that the content of Co on the surface of Co/CeO_2-NC catalyst was significantly lower than that of Co/CeO_2-3DOM catalyst. During the initial reaction rate range of the kinetic interval, the rate of reaction is not affected by diffusion, but only depends on the number and feature of active sites of the catalyst. The Co/CeO_2-3DOM catalyst gives relative higher TOF_{H2} values at 350 °C than the corresponding Co/CeO_2-NC catalyst. The reason of relatively low activity of Co/CeO_2-NC catalyst can be summarized as weaker electronic metal-support interaction and lower surface Co content. For CeO_2-based catalysts, increasing the surface oxygen storage capacity by controlling different morphologies means exposing more active surfaces [38]. The oxygen storage capacity is related to the surface composition of the catalyst. As shown in the XPS profiles in Fig. 4 and Table 2, the amount of surface oxygen vacancies of the Co/CeO_2-3DOM catalyst was relatively higher than that over the Co/CeO_2-NT and Co/CeO_2-NC catalysts. The H_2-TPR characterization results of CeO_2 support with different morphologies further verified this result.

The reaction mechanism of ammonia decomposition is explained in following steps: Firstly, ammonia is adsorbed to the active sites and then dissociated into adsorption of N and H atoms. In this process, adsorbed NH_3 is dehydrogenated to form NH_2* and H. Then NH_2* moves to a bridge site and dissociates to NH* and H. Secondly, N and H atoms recombine in the surface of active sites. Since N is present at the interstitial site after the dehydrogenation steps of NH*, and the energy barrier for associative desorption of N is critical. Therefore, nitrogen desorption is the rate-determining step. Finally, the recombinative N and H atoms desorb from the surface of active sites. The calculation of density functional theory (DFT) shows that the N atom desorption of ammonia at the Co active site is the slowest elementary step [39]. During ammonia decomposition, this leads to excessive accumulation of N atoms on the surface of the active site, resulting in decreased activity. Based on our previous understanding [40], the electron donating group (such as K^+) promotes the electron transfer between the active site and the support, resulting in a significant increase in the activity. The similar electron donation effects of Ce^{3+}/Ce^{4+} (or oxygen anion vacancy) occur on the oxygen anion vacancy. After the reduction of Co/CeO_2 catalysts by hydrogen at 600 °C, Co_3O_4 was reduced to Co metal and became the active site. In the process of ammonia decomposition, desorption of N from the Co-based catalyst surface is the key step to end the reaction. It is well known that the basicity of the support would lead to electron donation to metal, and the acidity would withdraw electrons to from metal. It has been reported in the literature [22,41] that basic dopants are used as promoters for ammonia decomposition to improve catalytic performance. Podila et al. [15] reported that the enhanced catalytic activity of cobalt-based catalyst was attributed to the improved basicity of catalysts. In fact, the surface oxygen vacancy can enhance the surface electron density of active sites and facilitate electrons from support to metal, inducing a decrease in the ionisation potential of the metal, thereby promoting the rebinding of N atoms adsorbed at the active site. CeO_2 supports with different morphologies can affect the number of surface oxygen vacancy, which is conducive to electron transfer at active sites, leading to different activities. It is summarized as the following formula (□ represents the oxygen anion vacancy):

$$Ce^{4+}(O^{2-})_{2-x}(e^-)_{2x} + Co = Ce^{4+}(O^{2-})_{2-x}(□)_{2x} + Co(e^-)_{2x} \quad (5)$$

Therefore, the high catalytic ammonia decomposition activity of Co/CeO_2 catalyst can be directly attributed to the fraction of more surface oxygen vacancies by changing the morphology of different CeO_2.

4. Conclusion

Co/CeO_2 catalysts with three-dimensional order mesoporous, nanotubes and nanocubes have been successfully prepared to elucidate the morphology-performance relationship for ammonia decomposition. Among all of them, the Co/CeO_2-3DOM catalyst shows the best catalytic performance than Co/CeO_2-NC and Co/CeO_2-NT catalysts. The active site of the three catalysts is similar. The size-dependent effect of Co/CeO_2 catalyst with nanoparticle size of 5.2–7.8 nm is not the main factor. Based on various characterization techniques, it can be concluded that the surface composition/electronic structure of CeO_2 with different morphologies is the main influencing factor, demonstrating the effect of morphological control is surface oxygen vacancies. High specific surface area and more surface oxygen vacancies are favorable for the construction of the more surface active sites on Co/CeO_2-3DOM catalyst. In addition, the Co/CeO_2-3DOM catalyst has 72 h of catalytic stability and reproducibility. The same strategy that morphological control greatly promotes the catalytic performance by enriching the surface-active sites can extend to other nano-catalysts for better understanding the structure-reactivity relationship.

CRediT authorship contribution statement

Chuanqing Huang: Data curation, Writing - original draft. **Yingzhi Yu:** Methodology, Software. **Xiaoyue Tang:** Software, Validation. **Zeyu**

Liu: Visualization, Investigation. **Jin Zhang:** Writing - review & editing. **Chuanzhen Ye:** Formal analysis. **Yong Ye:** Supervision. **Rongbin Zhang:** Conceptualization.

Declaration of Competing Interest

The authors declare that they have no known competing financial interests or personal relationships that could have appeared to influence the work reported in this paper.

Acknowledgements

This work was supported by the National Natural Science Foundation of China (No. 21868016), Natural Science Foundation Program of Guangdong Province (2018B030315010), Key R & D Program of Hunan Province (No. 2019NK2091), and National Key R & D Program of China (No. 2019YFD1002300).

References

[1] Y. Kojima, Hydrogen storage materials for hydrogen and energy carriers, Int. J. Hydrogen Energy 44 (2019) 18179–18192.
[2] A. Schneemann, J.L. White, S. Kang, S. Jeong, L.F. Wan, E.S. Cho, T.W. Heo, D. Prendergast, J.J. Urban, B.C. Wood, M.D. Allendorf, V. Stavila, Nanostructured metal hydrides for hydrogen storage, Chem. Rev. 118 (2018) 10775–10839.
[3] A. Klerke, C.H. Christensen, J.K. Norskov, T. Vegge, Ammonia for hydrogen storage: challenges and opportunities, J. Mater. Chem. 18 (2008) 2304–2310.
[4] S. Giddey, S.P.S. Badwal, C. Munnings, M. Dolan, Ammonia as a renewable energy transportation media, ACS Sustain. Chem. Eng. 5 (2017) 10231–10239.
[5] R. Lan, J.T.S. Irvine, S. Tao, Ammonia and related chemicals as potential indirect hydrogen storage materials, Int. J. Hydrogen Energy 37 (2012) 1482–1494.
[6] F. Schuth, R. Palkovits, R. Schlogl, D.S. Su, Ammonia as a possible element in an energy infrastructure: catalysts for ammonia decomposition, Energy Environ. Sci. 5 (2012) 6278–6289.
[7] S. Mukherjee, S.V. Devaguptapu, A. Sviripa, C.R.F. Lund, G. Wu, Low-temperature ammonia decomposition catalysts for hydrogen generation, Appl. Catal. B 226 (2018) 162–181.
[8] X. Ju, L. Liu, P. Yu, J. Guo, X. Zhang, T. He, G. Wu, P. Chen, Mesoporous Ru/MgO prepared by a deposition-precipitation method as highly active catalyst for producing CO_x-free hydrogen from ammonia decomposition, Appl. Catal. B 211 (2017) 167–175.
[9] I. Lucentini, A. Casanovas, J. Llorca, Catalytic ammonia decomposition for hydrogen production on Ni, Ru and NiRu supported on CeO_2, Int. J. Hydrogen Energy 44 (2019) 12693–12707.
[10] L. Li, Z.H. Zhu, Z.F. Yan, G.Q. Lu, L. Rintoul, Catalytic ammonia decomposition over Ru/carbon catalysts: the importance of the structure of carbon support, Appl. Catal. A 320 (2007) 166–172.
[11] L.H. Yao, Y.X. Li, J. Zhao, W.J. Ji, C.T. Au, Core–shell structured nanoparticles (M@SiO2, Al2O3, MgO; M = Fe Co, Ni, Ru) and their application in COx-free H2 production via NH3 decomposition, Catal. Today 158 (2010) 401–408.
[12] Q. Su, L. Gu, Y. Yao, J. Zhao, W. Ji, W. Ding, C.-T. Au, Layered double hydroxides derived $Ni_x(Mg_yAl_zO_n)$ catalysts: enhanced ammonia decomposition by hydrogen spillover effect, Appl. Catal. B 201 (2017) 451–460.
[13] Z.-P. Hu, L. Chen, C. Chen, Z.-Y. Yuan, Fe/ZSM-5 catalysts for ammonia decomposition to CO_x-free hydrogen: effect of SiO_2/Al_2O_3 ratio, Mol. Catal. 455 (2018) 14–22.
[14] L. Li, R. Jiang, W. Chu, H. Cang, H. Chen, J. Yan, Cobalt nanoparticles embedded in a porous carbon matrix as an efficient catalyst for ammonia decomposition, Catal. Sci. Tech. 7 (2017) 1363–1371.
[15] S. Podila, Y.A. Alhamed, A.A. AlZahrani, L.A. Petrov, Hydrogen production by ammonia decomposition using Co catalyst supported on Mg mixed oxide systems, Int. J. Hydrogen Energy 40 (2015) 15411–15422.
[16] H. Zhang, Y.A. Alhamed, W. Chu, Z. Ye, A. AlZahrani, L. Petrov, Controlling Co-support interaction in Co/MWCNTs catalysts and catalytic performance for hydrogen production via NH_3 decomposition, Appl. Catal. A 464–465 (2013) 156–164.
[17] Z. Lendzion-Bielun, U. Narkiewicz, W. Arabczyk, Cobalt-based catalysts for ammonia decomposition, Materials 6 (2013) 2400–2409.
[18] T.E. Bell, L. Torrente-Murciano, H_2 production via ammonia decomposition using non-noble metal catalysts: a review, Top. Catal. 59 (2016) 1438–1457.
[19] D. Varisli, N.G. Kaykac, Hydrogen from ammonia over cobalt incorporated silicate structured catalysts prepared using different cobalt salts, Int. J. Hydrogen Energy 41 (2016) 5955–5968.
[20] W. Zheng, J. Zhang, Q. Ge, H. Xu, W. Li, Effects of CeO_2 addition on Ni/Al_2O_3 catalysts for the reaction of ammonia decomposition to hydrogen, Appl. Catal. B 80 (2008) 98–105.
[21] X. Gong, Y.-Q. Gu, N. Li, H. Zhao, C.-J. Jia, Y. Du, Thermally stable hierarchical nanostructures of ultrathin MoS_2 nanosheet-coated CeO_2 hollow spheres as catalyst for ammonia decomposition, Inorg. Chem. 55 (2016) 3992–3999.
[22] L. Torrente-Murciano, A.K. Hill, T.E. Bell, Ammonia decomposition over cobalt/carbon catalysts-effect of carbon support and electron donating promoter on activity, Catal. Today 286 (2017) 131–140.
[23] S. Podila, H. Driss, S.F. Zaman, Y.A. Alhamed, A.A. AlZahrani, M.A. Daous, L.A. Petrov, Hydrogen generation by ammonia decomposition using $Co/MgO\text{-}La_2O_3$ catalyst: influence of support calcination atmosphere, J. Mol. Catal. A 414 (2016) 130–139.
[24] S.C. Laha, R. Ryoo, Synthesis of thermally stable mesoporous cerium oxide with nanocrystalline frameworks using mesoporous silica templates, Chem. Commun. (2003) 2138–2139.
[25] G. Chen, S. Sun, X. Sun, W. Fan, T. You, Formation of CeO_2 nanotubes from Ce $(OH)C_O3$ nanorods through kirkendall diffusion, Inorg. Chem. 48 (2009) 1334–1338.
[26] R. Zhang, K. Lu, L. Zong, S. Tong, X. Wang, G. Feng, Gold supported on ceria nanotubes for CO oxidation, Appl. Surf. Sci. 416 (2017) 183–190.
[27] R. Zhang, K. Lu, L. Zong, S. Tong, X. Wang, J. Zhou, Z.-H. Lu, G. Feng, Control synthesis of CeO_2 nanomaterials supported gold for catalytic oxidation of carbon monoxide, Mol. Catal. 442 (2017) 173–180.
[28] Z. Feng, Q. Ren, R. Peng, S. Mo, M. Zhang, M. Fu, L. Chen, D. Ye, Effect of CeO_2 morphologies on toluene catalytic combustion, Catal. Today 332 (2019) 177–182.
[29] F. Kleitz, S.H. Choi, R. Ryoo, Cubic Ia3d large mesoporous silica: synthesis and replication to platinum nanowires, carbon nanorods and carbon nanotubes, Chem. Commun. (2003) 2136–2137.
[30] M. Konsolakis, M. Sgourakis, S.A.C. Carabineiro, Surface and redox properties of cobalt–ceria binary oxides: on the effect of Co content and pretreatment conditions, Appl. Surf. Sci. 341 (2015) 48–54.
[31] G.H. Jaffari, A. Imran, M. Bah, A. Ali, A.S. Bhatti, U.S. Qurashi, S. Ismat Shah, Identification and quantification of oxygen vacancies in CeO_2 nanocrystals and their role in formation of F-centers, Appl. Surf. Sci. 396 (2017) 547–553.
[32] B. Bai, H. Arandiyan, J. Li, Comparison of the performance for oxidation of formaldehyde on nano-Co_3O_4, 2D-Co_3O_4, and 3D-Co_3O_4 catalysts, Appl. Catal. B 142–143 (2013) 677–683.
[33] C. Huang, H. Li, J. Yang, C. Wang, F. Hu, X. Wang, Z.-H. Lu, G. Feng, R. Zhang, $Ce_{0.6}Zr_{0.3}Y_{0.1}O_2$ solid solutions-supported Ni-Co bimetal nanocatalysts for NH_3 decomposition, Appl. Surf. Sci. 478 (2019) 708–716.
[34] J.M. López, A.L. Gilbank, T. García, B. Solsona, S. Agouram, L. Torrente-Murciano, The prevalence of surface oxygen vacancies over the mobility of bulk oxygen in nanostructured ceria for the total toluene oxidation, Appl. Catal. B 174–175 (2015) 403–412.
[35] H.A. Lara-García, J.A. Mendoza-Nieto, H. Pfeiffer, L. Torrente-Murciano, CO_x-free hydrogen production from ammonia on novel cobalt catalysts supported on 1D titanate nanotubes, Int. J. Hydrogen Energy 44 (2019) 30062–30074.
[36] J. Zhang, M. Comotti, F. Schüth, R. Schlögl, D.S. Su, Commercial Fe- or Co-containing carbon nanotubes as catalysts for NH_3 decomposition, Chem. Commun. (2007) 1916–1918.
[37] C.T. Campbell, Catalyst-support interactions: electronic perturbations, Nat. Chem. 4 (2012) 597–598.
[38] Z. Ma, S. Zhao, X. Pei, X. Xiong, B. Hu, New insights into the support morphology-dependent ammonia synthesis activity of Ru/CeO_2 catalysts, Catal. Sci. Tech. 7 (2017) 191–199.
[39] X. Duan, J. Ji, G. Qian, C. Fan, Y. Zhu, X. Zhou, D. Chen, W. Yuan, Ammonia decomposition on Fe(110), Co(111) and Ni(111) surfaces: a density functional theory study, J. Mol. Catal. A 357 (2012) 81–86.
[40] C. Huang, Y. Yu, J. Yang, Y. Yan, D. Wang, F. Hu, X. Wang, R. Zhang, G. Feng, Ru/La_2O_3 catalyst for ammonia decomposition to hydrogen, Appl. Surf. Sci. 476 (2019) 928–936.
[41] K. Nagaoka, T. Eboshi, N. Abe, S.-I. Miyahara, K. Honda, K. Sato, Influence of basic dopants on the activity of Ru/Pr_6O_{11} for hydrogen production by ammonia decomposition, Int. J. Hydrogen Energy 39 (2014) 20731–20735.
[42] X. Li, W. Ji, J. Zhao, S. Wang, C. Au, Ammonia decomposition over Ru and Ni catalysts supported on fumed SiO_2, MCM-41, and SBA-15, J. Catal. 236 (2005) 181–189.
[43] H. Zhang, Y.A. Alhamed, A. Al-Zahrani, M. Daous, H. Inokawa, Y. Kojima, L.A. Petrov, Tuning catalytic performances of cobalt catalysts for clean hydrogen generation via variation of the type of carbon support and catalyst post-treatment temperature, Int. J. Hydrogen Energy 39 (2014) 17573–17582.